



# CHORUS

This is the accepted manuscript made available via CHORUS. The article has been published as:

## Observation of Fermi arc and its connection with bulk states in the candidate type-II Weyl semimetal $\text{WTe}_2$

Chenlu Wang *et al.*

Phys. Rev. B **94**, 241119 — Published 30 December 2016

DOI: [10.1103/PhysRevB.94.241119](https://doi.org/10.1103/PhysRevB.94.241119)

# Observation of Fermi Arc and its Connection with Bulk States in the Candidate Type II Weyl Semimetal $\text{WTe}_2$

Chenlu Wang<sup>1,‡</sup>, Yan Zhang<sup>1,‡</sup>, Jianwei Huang<sup>1,‡</sup>, Simin Nie<sup>1</sup>, Guodong Liu<sup>1,\*</sup>,  
Aiji Liang<sup>1</sup>, Yuxiao Zhang<sup>1</sup>, Bing Shen<sup>1</sup>, Jing Liu<sup>1</sup>, Cheng Hu<sup>1</sup>, Ying Ding<sup>1</sup>,  
Defa Liu<sup>1</sup>, Yong Hu<sup>1</sup>, Shaolong He<sup>1</sup>, Lin Zhao<sup>1</sup>, Li Yu<sup>1</sup>, Jin Hu<sup>2</sup>, Jiang  
Wei<sup>2</sup>, Zhiqiang Mao<sup>2</sup>, Youguo Shi<sup>1</sup>, Xiaowen Jia<sup>3</sup>, Fengfeng Zhang<sup>4</sup>, Shenjin  
Zhang<sup>4</sup>, Feng Yang<sup>4</sup>, Zhimin Wang<sup>4</sup>, Qinjun Peng<sup>4</sup>, Hongming Weng<sup>1,6</sup>, Xi  
Dai<sup>1,6</sup>, Zhong Fang<sup>1,6</sup>, Zuyan Xu<sup>4</sup>, Chuangtian Chen<sup>4</sup> and X. J. Zhou<sup>1,5,6,\*</sup>

<sup>1</sup>*Beijing National Laboratory for Condensed Matter Physics,  
Institute of Physics, Chinese Academy of Sciences, Beijing 100190, China.*

<sup>2</sup>*Department of Physics and Engineering Physics,  
Tulane University, New Orleans, Louisiana 70118, USA*

<sup>3</sup>*Military Transportation University, Tianjin 300161, China.*

<sup>4</sup>*Technical Institute of Physics and Chemistry,  
Chinese Academy of Sciences, Beijing 100190, China.*

<sup>5</sup>*School of Physical Sciences, University of Chinese  
Academy of Sciences, Beijing 100190, China.*

<sup>6</sup>*Collaborative Innovation Center of Quantum Matter, Beijing 100871, China.*

<sup>‡</sup>*These people contributed equally to the present work.*

<sup>\*</sup>*Corresponding author: gdlou\_arpes@iphy.ac.cn, XJZhou@iphy.ac.cn.*

(Dated: August 21, 2016)

## Abstract

A new kind of topological materials, the type II Weyl semimetals, is proposed recently where the Weyl points emerge at the contact points of electron and hole pockets resulting in a highly tilted Weyl cone. In the type II Weyl semimetals, the Lorentz invariance is violated and a new kind of Weyl Fermions is generated that leads to new physical properties.  $\text{WTe}_2$  is interesting because it is predicted to be a good candidate of realizing type II Weyl semimetals. By utilizing laser-based angle-resolved photoemission spectroscopy with high energy and momentum resolutions, we have revealed a full picture on the electronic structure of  $\text{WTe}_2$ . Clear surface state has been identified and its connection with the bulk electronic states in the momentum and energy space shows a good agreement with the band structure calculations. Our results provide electronic signatures that are consistent with the type II Weyl states in  $\text{WTe}_2$ . They lay a foundation for further investigation on the topological nature of  $\text{WTe}_2$  and exploration of novel phenomena and physical properties in the type II Weyl semimetals.

PACS numbers:

The study of quantum topological materials has seen a rapid progress from the discovery of topological insulators[1, 2], to three-dimensional Dirac semimetals[3–11] and to three-dimensional Weyl semimetals[12–22]. These materials have attracted much attention because they represent new states of matter with unique electronic structure, spin texture and associated novel physical properties. The latest development is the further classification of the three-dimensional Weyl semimetals that results in the so-called “type II” Weyl semimetals[23] in addition to the well-known type I Weyl semimetals[12–22]. In the type I Weyl semimetals, a topologically protected linear crossing of two bands, i.e., a Weyl point, occurs at the Fermi level resulting in a point-like Fermi surface. In this new type II Weyl semimetals, the Weyl points emerge at the contact points of electron and hole pockets resulting in a highly tilted Weyl cone. The Lorentz invariance is violated in the type II Weyl semimetals and a fundamentally new kind of Weyl Fermions is produced that leads to new physical properties[23].

WTe<sub>2</sub> has been well-known for its manifestation of extremely large magnetoresistance that is attributed to the compensation of electrons and holes in the material[24]. Various alternative mechanisms have been proposed later on to account for the anomalous transport properties of WTe<sub>2</sub>[25–29]. A complete understanding of the electronic structure of WTe<sub>2</sub> is a prerequisite to pin down the origin of its anomalous transport properties. However, due to the existence of multiple pockets in a limited momentum space, the full electronic structure picture of WTe<sub>2</sub> remains controversial[30–34]. Lately, WTe<sub>2</sub> has ignited another surge of excitement because it is theoretically predicted to be the first material candidate that may realize type-II Weyl state[23]. It has motivated exploration of type II semimetal state in other candidates like MoTe<sub>2</sub> and (Mo,W)Te<sub>2</sub> which are isostructural with WTe<sub>2</sub>[23, 35–38]. However, so far experimental evidence on the identification of type II Weyl Fermions in WTe<sub>2</sub> is still lacking.

In this work, we report our combined experimental and theoretical investigations on the complete picture of the electronic structure of WTe<sub>2</sub>. Taking advantage of our latest generation laser-based angle-resolved photoemission (ARPES) system that can cover two-dimensional momentum space simultaneously with high energy and momentum resolutions, we have revealed a full picture on the electronic structure of WTe<sub>2</sub>. We have identified the existence of surface state that connects the bulk electron and hole pockets. High temperature ARPES measurements make us possible to reveal electronic states above the Fermi level

where the Weyl points are predicted to be located. The observed connection of the surface state with the bulk bands, its momentum evolution, its momentum and energy locations, are all in good agreement with the calculated band structures. Our results provide electronic signatures that are consistent with the type II Weyl state in  $\text{WTe}_2$  although further efforts are needed to fully prove the realization of type II Weyl state in  $\text{WTe}_2$ .

$\text{WTe}_2$  is a layered compound which crystallizes in the Td type of orthorhombic crystal structure that is constructed from layer-stacking along the  $c$ -axis of the two-dimensional  $\text{WTe}_2$  sheets (as seen in Fig. 1a)[39]. The  $\text{WTe}_2$  single crystals were grown via two different approaches. One is the chemical vapour transport method and the other is the self-flux method with Tellurium as the solvent. In the chemical vapor method, high quality  $\text{WTe}_2$  single crystals were synthesized with stoichiometric mixture of W/Te powder, using the chemical vapor transport with iodine as the transport agent. During the crystal growth, the temperature was set at 900 °C and 800 °C, respectively, for the hot and cold ends of the double zone tube furnace. The sheet-like single crystals with metal luster can be obtained at the cold zone after one week growth.

The ARPES measurements were performed using our newly-developed laser-based ARPES system equipped with the 6.994 eV vacuum-ultra-violet (VUV) laser and the time-of-flight electron energy analyzer (ARToF10K by Scienta Omicron). This ARPES system is capable of measuring photoelectrons covering two-dimensional momentum space ( $k_x, k_y$ ) simultaneously. Measurements were performed using both  $s$ - and  $p$ -polarization geometries. In the  $s$ -polarization geometry, the electric field vector of the incident laser is perpendicular to the plane formed by the incident light and the lens axis of the electron energy analyzer, while in the  $p$ -polarization geometry, the electric field vector of the incident light lies within such a plane. Because photoemission process involves matrix element effects that enhance or suppress the signal of each bands, our measurements under two distinct polarization geometries provide complementary information to fully reveal the electronic structures of the measured  $\text{WTe}_2$  samples. The overall energy resolution was set at 1~5 meV, and the angular resolution was  $\sim 0.1^\circ$ . All the samples were cleaved *in situ* at 20 K and measured in ultra-high vacuum with a base pressure better than  $5 \times 10^{-11}$  mbar. The Fermi level is referenced by measuring on a clean polycrystalline gold that is electrically connected to the sample. We performed ARPES experiments on many pieces of  $\text{WTe}_2$  crystals prepared by both the vapor transport method and the self-flux method. The measured results are consistent for

these two kinds of WTe<sub>2</sub> samples.

The electronic structure calculations are performed by using the projector augmented wave (PAW) method[40, 41] as implemented in the Vienna *ab initio* simulation package (VASP)[42, 43]. The experimental lattice constants at 113 K ( $a=3.477\text{\AA}$ ,  $b=6.249\text{\AA}$  and  $c=14.018\text{\AA}$ )[44] are employed in the electronic structure calculations. The exchange and correlation effects are treated using the generalized gradient approximation (GGA)[45]. Spin-orbit-coupling is taken into account in the self-consistent iterations. The integration is done on a grid of k points with the size  $13\times 9\times 4$ . The plane wave cut-off energy of 500 eV is used. The maximally localized Wannier functions (MLWFs) for the *d* orbitals of W atoms and *p* orbitals of Te atoms have been constructed by using the WANNIER90 code[46–48]. The topological surface states have been calculated by using the Wannier functions.

Depending on different cleavage surfaces and different measurement conditions, we have resolved three forms of distinct electronic structures on WTe<sub>2</sub> (see Fig. S1 in Supplementary Materials). The Form 1 is observed most often during the experiments (Among 12 WTe<sub>2</sub> samples we measured, 9 of them exhibit similar electronic structures shown as Form 1 in Fig. S1 of Supplementary Materials). This Form 1 is also the same electronic structure form where the type II Weyl semimetal state is predicted in WTe<sub>2</sub>[23]. Therefore, we will focus on this electronic structure form in the main text below.

Figure 1(d,e) show the Fermi surface of WTe<sub>2</sub> measured at 20 K under two distinct *p*- and *s*-polarization geometries. The corresponding constant energy contours at different binding energies are shown in Fig. 1(i,j). For comparison, the calculated bulk Fermi surface, and the Fermi surface including the surface state, are shown in Fig. 1g and Fig. 1h, respectively. The band structures along some representative momentum cuts and around some particular momentum space are shown in Fig. 2. The analysis of the constant energy contours at different binding energies (Fig. 1) and the band structures along some typical momentum cuts (Fig. 2), compared with band structure calculations, provides a measured Fermi surface picture of WTe<sub>2</sub>, as schematically shown in Fig. 1f. The observed electronic structures can be summarized as the following. (1). Four hole pockets are resolved, labeled as  $\alpha$ ,  $\beta$  and two nearly degenerate hole pockets  $\gamma$  and  $\gamma'$  in Fig. 1f, with their corresponding bands shown in Cut 5 panel of Fig. 2b. (2). Two electron pockets which are nearly degenerate can be resolved as  $\delta$  and  $\epsilon$  in Fig. 1f (see Fig. S3 in Supplementary Materials) and their corresponding bands marked in Cut 5 panel of Fig. 2b. With increasing binding energy, the

hole pockets ( $\alpha$ ,  $\beta$ ,  $\gamma$  and  $\gamma'$ ) expand while the electron pockets ( $\delta$  and  $\epsilon$ ) shrink, as seen from Fig. 1i and 1j, consistent with their assignments. (3). There is spectral weight near  $\Gamma$  in the measurement under  $s$ -polarization geometry (Fig. 1e) that is strongly suppressed in the measurement under  $p$ -polarization geometry (Fig. 1d). A flat band can be observed near  $\Gamma$  in Cut 5 panel of Fig. 2d. Analysis of the EDC at  $\Gamma$  point indicates that this band top is about 5 meV below the Fermi level (see Fig. S2 in Supplementary Materials); therefore it does not form a Fermi surface sheet at  $\Gamma$ . With increasing binding energy, it shows up as a hole pocket and grows in its area, as seen in Fig. 1i and 1j. (4). A prominent feature in the measured Fermi surface is the V-shaped SS1 segment that connects the hole pockets and electron pockets in Fig. 1d and 1e. It keeps in contact with the electron pocket with increasing binding energy but gradually detaches from the hole pockets (Fig. 1(i, j)). This feature is not present in the calculated bulk Fermi surface (Fig. 1g) and bulk band structure (Fig. 2e), but it is consistent with the band structure calculations including the surface state (Fig. 1h and Fig. 2f). The good agreement between the measured and calculated Fermi surface (Fig. 1(d,e) and Fig. 1h), as well as between the measured and calculated band structures (Cut 5 panels of Fig. 2(b, d) and Fig. 2f), indicates that this SS1 feature represents the surface state expected from the band structure calculations. (5). In the calculated band structures (Fig. 2f), there is another surface state band ss2. But this band is clear only above the Fermi level and merges into bulk bands below the Fermi level. Therefore, this ss2 surface band is not clearly resolved in our measurements (Cut 5 panels of Fig. 2(b, d)).

Our high resolution laser ARPES measurements provide a full picture on the electronic structure of  $\text{WTe}_2$  which helps address issues in literatures due to unresolved fine structures or band mis-assignments. It is clear that, within the similar energy range, we have resolved more complete bands than reported before in  $\text{WTe}_2$ [26, 34, 49, 50]. The agreement between our experiments and the band structure calculations provides a clear identification of most of the observed bands in  $\text{WTe}_2$ . The absence of the  $\gamma$  and  $\gamma'$  hole pockets in the calculations (Fig. 1g) could be due to a chemical potential difference; a slight shifting down of the chemical potential can produce the third hole pocket in the calculations (see Fig. S2 in Supplementary Materials). In particular, the observation and assignment of the surface state SS1 is important for examining the electron-hole compensation picture in understanding the anomalously large magnetoresistance in  $\text{WTe}_2$  because it was previously either not resolved

or assigned incorrectly as a bulk band[26, 34, 49, 50]. According to our results, we obtain hole concentration of  $0.017\text{\AA}^{-2}$  ( $\alpha$ ),  $0.013\text{\AA}^{-2}$  ( $\beta$ ),  $0.005\text{\AA}^{-2}$  ( $\gamma$ ) and  $0.005\text{\AA}^{-2}$  ( $\gamma'$ ) for the four hole pockets and electron concentration of  $0.009\text{\AA}^{-2}$  ( $\delta$ ) and  $0.008\text{\AA}^{-2}$  ( $\epsilon$ ) for the two electron pockets. The overall hole concentration is apparently larger than that of the overall electron concentration, asking for the re-examination of the electron-hole compensation picture for understanding the anomalous transport properties in  $\text{WTe}_2$ [24]. However, according to the previous calculations and measurements[24, 51], the bulk bands of  $\text{WTe}_2$  are three dimensional. This should be taken into consideration when determining the balance of electrons and holes from the Luttinger volume. Also, the strong spin orbital coupling and the lack of inversion symmetry in  $\text{WTe}_2$ , which break the spin-degeneracy of the Fermi surface sheets, should be considered in affecting the magnetoresistance of  $\text{WTe}_2$ [26]. In addition, the flat band very close to the Fermi level at  $\Gamma$  (Cut 5 panel of Fig. 2d) may also play an important role in dictating the transport properties of  $\text{WTe}_2$ . Therefore, the exact origin of the extraordinary magnetoresistance in  $\text{WTe}_2$  deserves further investigations.

Our high-resolution ARPES results also make it possible to compare with the band structure calculations in order to examine the topological nature of  $\text{WTe}_2$  as theoretically predicted[23]. The observation of the SS1 surface state is in agreement with the theoretical expectation of the type II Weyl Fermions in  $\text{WTe}_2$ [23]. Fig. 2h and 2j show detailed band structure evolution with momentum covering the momentum space where the surface state SS1, the bulk electron pockets and hole pockets are all seen. Along  $\Gamma$ -X direction (Cut 1), the surface state band ss1 comes out of the electron band  $\delta$  at a binding energy of  $\sim 80$  meV. It nearly overlaps with the hole band  $\alpha$  at the Fermi level. With the momentum cuts moving away from the  $\Gamma$ -X direction, the surface state band ss1 and the hole band  $\alpha$  separate at the Fermi level, while it moves up in energy, gradually approaches the electron band  $\delta$ , overlaps and eventually disappears when the momentum cut moves away from the electron pocket window (Cut 6). This evolution can also be clearly seen from constant energy contours at different binding energies (Fig. 1i and 1j). At high binding energies, the surface state SS1 connects to the electron pocket  $\delta$ . With the decrease of the binding energy, the V-shaped surface state bottom tip gradually approaches the hole pocket  $\alpha$  around the Fermi level. Therefore, the surface state SS1 connects the electron pocket and hole pocket, as expected from the band structure calculations[23].

According to our band structure calculations, there are four pairs of type II Weyl points

(W1,W2) in WTe<sub>2</sub> on the  $k_z = 0$  plane, as shown in Fig. 3d in the momentum space that is consistent with the previous calculations[23]. The W1 Weyl point is located 56 meV above the Fermi level while the other W2 Weyl point is 89 meV above the Fermi level (Fig. 3g). Two surface state bands are expected, ss1 and ss2, as also expected before[23, 35, 36]. Along the  $\Gamma$ -X direction (Fig. 3c, Cut 1), the surface state band ss1 comes out of the electron band  $\delta$  and merges into the hole band  $\alpha$ . When the momentum cuts move away from the  $\Gamma$ -X direction (Fig. 3c, Cut 2), the electron pocket and hole pocket touch at the first Weyl point W1 and the surface state joins the W1 Weyl points. After that (Fig. 3c, Cut 3), the surface state ss1 comes out of the electron band and goes back to the electron band. The other surface state ss2 connects the hole band and electron band at even higher energy. Further increase of  $k_y$  (Fig. 3c, Cut 4) results in the second touching of electron and hole pockets at the Weyl point W2 where the surface state ss2 merges into the bulk band. Eventually (Fig. 3c, Cut 5), the electron band and hole band separate again, and the surface state ss1 comes from the electron band and goes back to this band. The predicted momentum evolution of the surface state bands and Weyl points provides clear signatures for experiments to compare.

In order to reveal the Weyl points that lie above the Fermi level, we carried out high resolution ARPES measurements on WTe<sub>2</sub> at high temperatures (up to 200 K), which makes it possible to observe electronic states above the Fermi level due to thermal excitations. Fig. 3a and 3b show band structures of WTe<sub>2</sub> at 100 K and 200 K, respectively, measured along  $\Gamma$ -X direction with different  $k_y$ s that cover the momentum and energy window of the Weyl points. Although the signal is relatively weak in this case simply because it is from thermal excitations, and the data are not clear enough to resolve individual W1 and W2 Weyl points, the overall agreement between the measurements (Fig. 3a and 3b) and calculations (Fig. 3c) is remarkable in two aspects. First, the top of the hole bands (Fig. 3a and 3b) is revealed and its location is rather similar to that expected in the band structure calculations (Fig. 3c). Second, the overall momentum evolution of the surface state ss1 shows a good agreement with the band structure calculations. Along  $\Gamma$ -X (Fig. 3a and 3b, Cut 1), the surface state ss1 comes out of the electron band and merges into the hole band. When the momentum cut moves away from  $\Gamma$ -X, the ss1 surface state moves up in energy. When it comes to momentum Cut 5 (Fig. 3a and 3b), it becomes clear that the surface state ss1 comes out from the electron band and merges back to the electron band that is consistent with the

band structure calculations (Cut 5 of Fig. 3c).

The overall agreement between our measurements and band structure calculations can also be seen from the constant energy contours of  $\text{WTe}_2$ , as shown in Fig. 4. Fig. 4c shows the calculated constant energy contours covering the energy window of the Weyl points. The surface state SS1 comes out from the electron pocket and merges into the hole pocket at low energy (Fig. 4c,  $E = 50$  meV). With an increase of energy to  $E=56$  meV (Fig. 4c,  $E=56$  meV), the surface state SS1 comes out from the electron pocket, and gets connected with the W1 Weyl point. With the further increase of energy, the surface state SS1 comes from the electron pocket and merges into the electron band (Fig. 4c, 60 meV). In the meantime, another surface state SS2 appears at the W2 Weyl point (Fig. 4c, 89 meV), and merges fully into the electron pocket (Fig. 4c, 100 meV). The measured constant energy contours of  $\text{WTe}_2$  at 100 K (Fig. 4a) and 200 K (Fig. 4b) above the Fermi level exhibit qualitative agreement with the band structure calculations (Fig. 4c). At a relatively low energy 20 meV (Fig. 4a and 4b, 20 meV panels), the surface state SS1 comes out from the electron pocket and merges into the hole pocket. But when it comes to 50 meV (Fig. 4a and 4b), with the vanishing of the hole pocket, the surface state SS1 comes out from the electron pocket and goes back to the electron pocket, showing a good agreement with theoretical calculations.

As demonstrated before, small changes in the lattice parameters of  $\text{MoTe}_2$  or  $\text{WTe}_2$  can dramatically change the nature of the calculated band structure[23, 35–38, 51]. Calculations for the low and high temperature lattice parameters of  $\text{WTe}_2$  produce a band structure with 8 and 0 Weyl points, respectively[51]. It is further shown that the surface state SS1 in a calculation with 0 Weyl point and 8 Weyl points is very similar and any differences in its dispersion are beyond the resolution of our ARPES experiments. This is consistent with our observation of similar results measured at 20, 100 and 200 K, a temperature range for which lattice parameter variations have been reported. Therefore, although our observation of the SS1 Fermi arc and its connection with the bulk states are consistent with  $\text{WTe}_2$  being a type II Weyl semimetal, they do not constitute sufficient evidence at present to prove that  $\text{WTe}_2$  is a type II Weyl semimetal.

In summary, by taking high resolution ARPES measurements and performing band structure calculations, we have provided a complete picture on the electronic structure of  $\text{WTe}_2$ . We have clearly identified a surface state that connects the electron pocket and hole pocket. Above the Fermi level and in the momentum space where the type II Weyl points are ex-

pected, our experimental results show a good agreement with the band structure calculations on the relation between the surface state and bulk band states. These observations, and their overall agreement with theoretical calculations, provide electronic signatures that are consistent with the type II Weyl state in  $\text{WTe}_2$ . Further investigations are needed to fully prove the realization of type II Weyl state in  $\text{WTe}_2$  by resolving Weyl points W1 and W2 clearly.

*Note added.* After completion of the paper, we become aware of several ARPES results on  $\text{MoTe}_2$ [52–57] and  $\text{WTe}_2$ [58–60] in which similar Fermi arcs were observed that are consistent with our results.

- 
- [1] M. Z. Hasan, and C. L. Kane, *Rev. Mod. Phys.* **82**, 3045 (2010).
  - [2] X. L. Qi, and S. C. Zhang, *Rev. Mod. Phys.* **83**, 1057 (2011).
  - [3] Z. Wang, Y. Sun, X.-Q. Chen, C. Franchini, G. Xu, H. Weng, X. Dai, and Z. Fang, *Phys. Rev. B* **85**, 195320 (2012).
  - [4] Z. K. Liu, B. Zhou, Y. Zhang, Z. J. Wang, H. M. Weng, D. Prabhakaran, S.-K. Mo, Z. X. Shen, Z. Fang, X. Dai, Z. Hussain, and Y. L. Chen, *Science* **343**, 864 (2014).
  - [5] S.-Y. Xu, C. Liu, S. K. Kushwaha, R. Sankar, J. W. Krizan, I. Belopolski, M. Neupane, G. Bian, N. Alidoust, T.-R. Chang, H.-T. Jeng, C.-Y. Huang, W.-F. Tsai, H. Lin, P. P. Shibayev, F.-C. Chou, R. J. Cava, and M. Z. Hasan, *Science* **347**, 294 (2015).
  - [6] A. Liang, C. Chen, Z. Wang, Y. Shi, Y. Feng, H. Yi, Z. Xie, S. He, J. He, Y. Peng, Y. Liu, D. Liu, C. Hu, L. Zhao, G. Liu, X. Dong, J. Zhang, M. Nakatake, H. Iwasawa, K. Shimada, M. Arita, H. Namatame, M. Taniguchi, Z. Xu, C. Chen, H. Weng, X. Dai, Z. Fang, X. J. Zhou, *Chin. Phys. B* **25**, 077101 (2016).
  - [7] Z. Wang, H. Weng, Q. Wu, X. Dai, and Z. Fang, *Phys. Rev. B* **88**, 125427 (2013).
  - [8] Z. K. Liu, J. Jiang, B. Zhou, Z. J. Wang, Y. Zhang, H. M. Weng, D. Prabhakaran, S.-K. Mo, H. Peng, P. Dudin, T. Kim, M. Hoesch, Z. Fang, X. Dai, Z. X. Shen, D. L. Feng, Z. Hussain, and Y. L. Chen, *Nat. Mater.* **13**, 677 (2014).
  - [9] M. Neupane, S.-Y. Xu, R. Sankar, N. Alidoust, G. Bian, C. Liu, I. Belopolski, T.-R. Chang, H.-T. Jeng, H. Lin, A. Bansil, F. Chou, and M. Z. Hasan, *Nat. Commun.* **5**, 3786 (2014).

- [10] S. Borisenko, Q. Gibson, D. Evtushinsky, V. Zabolotnyy, B. Büchner, and R. J. Cava, *Phys. Rev. Lett.* **113**, 027603 (2014).
- [11] H. Yi, Z. Wang, C. Chen, Y. Shi, Y. Feng, A. Liang, Z. Xie, S. He, J. He, Y. Peng, X. Liu, Y. Liu, L. Zhao, G. Liu, X. Dong, J. Zhang, M. Nakatake, M. Arita, K. Shimada, H. Namatame, M. Taniguchi, Z. Xu, C. Chen, X. Dai, Z. Fang, and X. J. Zhou, *Sci. Rep.* **4**, 6106 (2014).
- [12] H. Weyl, *Z. Phys.* **56**, 330 (1929).
- [13] H. B. Nielsen, and M. Ninomiya, *Phys. Lett. B* **130**, 389 (1983).
- [14] S. Murakami, *New J. Phys.* **9**, 356 (2007).
- [15] X. Wan, A. M. Turner, A. Vishwanath, and S. Y. Savrasov, *Phys. Rev. B* **83**, 205101 (2011).
- [16] A. A. Burkov, and L. Balents, *Phys. Rev. Lett.* **107**, 127205 (2011).
- [17] G. Xu, H. Weng, Z. Wang, X. Dai, and Z. Fang, *Phys. Rev. Lett.* **107**, 186806 (2011).
- [18] S.-M. Huang, S.-Y. Xu, I. Belopolski, C.-C. Lee, G. Chang, B. Wang, N. Alidoust, G. Bian, M. Neupane, C. Zhang, S. Jia, A. Bansil, H. Lin, and M. Z. Hasan, *Nat. Commun.* **6**, 7373 (2015).
- [19] H. Weng, C. Fang, Z. Fang, B. A. Bernevig, and X. Dai, *Phys. Rev. X* **5**, 011029 (2015).
- [20] S.-Y. Xu, I. Belopolski, N. Alidoust, M. Neupane, G. Bian, C. Zhang, R. Sankar, G. Chang, Z. Yuan, C.-C. Lee, S.-M. Huang, H. Zheng, J. Ma, D. S. Sanchez, B. Wang, A. Bansil, F. Chou, P. P. Shibayev, H. Lin, S. Jia, and M. Z. Hasan, *Science* **349**, 613 (2015).
- [21] B. Q. Lv, H. M. Weng, B. B. Fu, X. P. Wang, H. Miao, J. Ma, P. Richard, X. C. Huang, L. X. Zhao, G. F. Chen, Z. Fang, X. Dai, T. Qian, and H. Ding, *Phys. Rev. X* **5**, 031013 (2015).
- [22] L. X. Yang, Z. K. Liu, Y. Sun, H. Peng, H. F. Yang, T. Zhang, B. Zhou, Y. Zhang, Y. F. Guo, M. Rahn, D. Prabhakaran, Z. Hussain, S.-K. Mo, C. Felser, B. Yan, and Y. L. Chen, *Nature Phys.* **11**, 728 (2015).
- [23] A. A. Soluyanov, D. Gresch, Z. Wang, Q. Wu, M. Troyer, X. Dai, and B. A. Bernevig, *Nature (London)* **527**, 495 (2015).
- [24] M. N. Ali, J. Xiong, S. Flynn, J. Tao, Q. D. Gibson, L. M. Schoop, T. Liang, N. Hal-  
dolaarachchige, M. Hirschberger, N. P. Ong, and R. J. Cava, *Nature (London)* **514**, 205 (2014).
- [25] X.-C. Pan, Y. Pan, J. Jiang, H. Zuo, H. Liu, X. Chen, Z. Wei, S. Zhang, Z. Wang, X. Wan, Z. Yang, D. Feng, Z. Xia, L. Li, F. Song, B. Wang, Y. Zhang, and G. Wang, *Front. Phys.* **12(3)**, 127203 (2017).

- [26] J. Jiang, F. Tang, X. C. Pan, H. M. Liu, X. H. Niu, Y. X. Wang, D. F. Xu, H. F. Yang, B. P. Xie, F. Q. Song, P. Dudin, T. K. Kim, M. Hoesch, P. K. Das, I. Vobornik, X. G. Wan, and D. L. Feng, *Phys. Rev. Lett.* **115**, 166601 (2015).
- [27] Y. Luo, H. Li, Y. Dai, H. Miao, Y. Shi, H. Ding, A. J. Taylor, D. A. Yarotski, R. P. Prasankumar, and J. D. Thompson, *Appl. Phys. Lett.* **107**, 182411 (2015).
- [28] D. Rhodes, S. Das, Q. R. Zhang, B. Zeng, N. R. Pradhan, N. Kikugawa, E. Manousakis, and L. Balicas, *Phys. Rev. B* **92**, 125152 (2015).
- [29] Y. Wang, K. Wang, J. R.-Robey, J. Paglione, and M. S. Fuhrer, *Phys. Rev. B* **93**, 121108(R) (2016).
- [30] Z. Zhu, X. Lin, J. Liu, B. Fauque, Q. Tao, C. Yang, Y. Shi, and K. Behnia, *Phys. Rev. Lett.* **114**, 176601 (2015).
- [31] Y. Zhao, H. Liu, J. Yan, W. An, J. Liu, X. Zhang, H. Wang, Y. Liu, H. Jiang, Q. Li, Y. Wang, X.-Z. Li, D. Mandrus, X. C. Xie, M. Pan, and J. Wang, *Phys. Rev. B* **92**, 041104(R) (2015).
- [32] F.-X. Xiang, M. Veldhorst, S.-X. Dou, and X.-L. Wang, *Europhys. Lett.* **112**, 37009 (2015).
- [33] P. L. Cai, J. Hu, L. P. He, J. Pan, X. C. Hong, Z. Zhang, J. Zhang, J. Wei, Z. Q. Mao, and S. Y. Li, *Phys. Rev. Lett.* **115**, 057202 (2015).
- [34] I. Pletikosić, M. N. Ali, A. V. Fedorov, R. J. Cava, and T. Valla, *Phys. Rev. Lett.* **113**, 216601 (2014).
- [35] Y. Sun, S.-C. Wu, M. N. Ali, C. Felser, and B. Yan, *Phys. Rev. B* **92**, 161107 (2015).
- [36] T.-R. Chang, S.-Y. Xu, G. Chang, C.-C. Lee, S.-M. Huang, B. Wang, G. Bian, H. Zheng, D. S. Sanchez, I. Belopolski, N. Alidoust, M. Neupane, A. Bansil, H.-T. Jeng, H. Lin, and M. Z. Hasan, *Nat. Commun.* **7**, 10639 (2016).
- [37] Z. Wang, D. Gresch, A. A. Soluyanov, W. Xie, S. Kushwaha, X. Dai, M. Troyer, R. J. Cava, and B. A. Bernevig, *Phys. Rev. Lett.* **117**, 056805 (2016).
- [38] I. Belopolski, S.-Y. Xu, Y. Ishida, X. Pan, P. Yu, D. S. Sanchez, H. Zheng, M. Neupane, N. Alidoust, G. Chang, T.-R. Chang, Y. Wu, G. Bian, S.-M. Huang, C.-C. Lee, D. Mou, L. Huang, Y. Song, B. Wang, G. Wang, Y.-W. Yeh, N. Yao, J. E. Rault, P. L. Fèvre, F. Bertran, H.-T. Jeng, T. Kondo, A. Kaminski, H. Lin, Z. Liu, F. Song, S. Shin, and M. Z. Hasan, *Phys. Rev. B* **94**, 085127 (2016).
- [39] B. E. Brown, *Acta. Cryst.* **20**, 268 (1966).
- [40] P. E. Blöchl, *Phys. Rev. B* **50**, 17953 (1994).

- [41] G. Kresse, and D. Joubert, *Phys. Rev. B* **59**, 1758 (1999).
- [42] G. Kresse, and J. Furthmüller, *Computational Materials Science* **6**, 15 (1996).
- [43] G. Kresse, and J. Furthmüller, *Phys. Rev. B* **54**, 11169 (1996).
- [44] A. Mar, S. Jobic, and J. A. Ibers, *J. Am. Chem. Soc.* **114**, 8963 (1992).
- [45] J. P. Perdew, K. Burke, and M. Ernzerhof, *Phys. Rev. Lett.* **77**, 3865 (1996).
- [46] N. Marzari, and D. Vanderbilt, *Phys. Rev. B* **56**, 12847 (1997).
- [47] I. Souza, N. Marzari, and D. Vanderbilt, *Phys. Rev. B* **65**, 035109 (2001).
- [48] A. A. Mostofi, J. R. Yates, Y.-Su. Lee, I. Souza, D. Vanderbilt, and N. Marzari, *Computer Physics Communications* **178**, 685 (2008).
- [49] Y. Wu, N. H. Jo, M. Ochi, L. Huang, D. Mou, S. L. Bud'ko, P. C. Canfield, N. Trivedi, R. Arita, and A. Kaminski, *Phys. Rev. Lett.* **115**, 166602 (2015).
- [50] J. Augustin, V. Eyert, Th. Böker, W. Frentrup, H. Dwelk, C. Janowitz, and R. Manzke, *Phys. Rev. B* **62**, 10812 (2000).
- [51] F. Y. Bruno, A. Tamai, Q. S. Wu, I. Cucchi, C. Barreteau, A. de la Torre, S. M. Walker, S. Riccò, Z. Wang, T. K. Kim, M. Hoesch, M. Shi, N. C. Plumb, E. Giannini, A. A. Soluyanov, and F. Baumberger, *Phys. Rev. B* **94**, 121112(R) (2016).
- [52] L. Huang, T. M. McCormick, M. Ochi, Z. Zhao, M. Suzuki, R. Arita, Y. Wu, D. Mou, H. Cao, J. Yan, N. Trivedi, and A. Kaminski, *Nat. Mater.* **15**, 1155 (2016).
- [53] K. Deng, G. Wan, P. Deng, K. Zhang, S. Ding, E. Wang, M. Yan, H. Huang, H. Zhang, Z. Xu, J. Denlinger, A. Fedorov, H. Yang, W. Duan, H. Yao, Y. Wu, S. Fan, H. Zhang, X. Chen, and S. Zhou, *Nat. Phys.* **12**, 1105 (2016).
- [54] J. Jiang, Z. K. Liu, Y. Sun, H. F. Yang, R. Rajamathi, Y. P. Qi, L. X. Yang, C. Chen, H. Peng, C.-C. Hwang, S. Z. Sun, S.-K. Mo, I. Vobornik, J. Fujii, S. S. P. Parkin, C. Felser, B. H. Yan, and Y. L. Chen, *arXiv:1604.00139* (2016).
- [55] A. Liang, J. Huang, S. Nie, Y. Ding, Q. Gao, C. Hu, S. He, Y. Zhang, C. Wang, B. Shen, J. Liu, P. Ai, L. Yu, X. Sun, W. Zhao, S. Lv, D. Liu, C. Li, Y. Zhang, Y. Hu, Y. Xu, L. Zhao, G. Liu, Z. Mao, X. Jia, F. Zhang, S. Zhang, F. Yang, Z. Wang, Q. Peng, H. Weng, X. Dai, Z. Fang, Z. Xu, C. Chen, and X. J. Zhou, *arXiv:1604.01706* (2016).
- [56] N. Xu, Z. J. Wang, A. P. Weber, A. Magrez, P. Bugnon, H. Berger, C. E. Matt, J. Z. Ma, B. B. Fu, B. Q. Lv, N. C. Plumb, M. Radovic, E. Pomjakushina, K. Conder, T. Qian, J. H. Dil, J. Mesot, H. Ding, and M. Shi, *arXiv:1604.02116* (2016).

- [57] A. Tamai, Q. S. Wu, I. Cucchi, F. Y. Bruno, S. Riccò, T. K. Kim, M. Hoesch, C. Barreteau, E. Giannini, C. Besnard, A. A. Soluyanov, and F. Baumberger, *Phys. Rev. X* **6**, 031021 (2016).
- [58] Y. Wu, D. Mou, N. H. Jo, K. Sun, L. Huang, S. L. Bud'ko, P. C. Canfield, and A. Kaminski, *Phys. Rev. B* **94**, 121113(R) (2016).
- [59] B. Feng, Y.-H. Chan, Y. Feng, R.-Y. Liu, M.-Y. Chou, K. Kuroda, K. Yaji, A. Harasawa, P. Moras, A. Barinov, W. G. Malaeb, C. Bareille, T. Kondo, S. Shin, F. Komori, T.-C. Chiang, Y. Shi, and I. Matsuda, *Phys. Rev. B* **94**, 195134 (2016).
- [60] J. Sánchez-Barriga, M. G. Vergniory, D. Evtushinsky, I. Aguilera, A. Varykhalov, S. Blügel, and O. Rader, *Phys. Rev. B* **94**, 161401(R) (2016).

### **Acknowledgement**

This work is supported by the National Science Foundation of China (11574367), the 973 project of the Ministry of Science and Technology of China (2013CB921904 and 2015CB921300), the National Key Research and Development Program of China (2016YFA0300600) and the Strategic Priority Research Program (B) of the Chinese Academy of Sciences (Grant No. XDB07020300). The work at Tulane is supported by the US Department of Energy under Grant DE-SC0014208.

### **Author Contributions**

C.L.W., Y.Z. and J.W.H. contribute equally to this work. X.J.Z. and G.D.L. proposed and designed the research. J.H., J.W., Z.Q.M. and Y.G.S. contributed in sample growth. S.M.N., H.W.M., X.D. and Z.F. contributed in the band structure calculations. C.L.W., Y.Z., J.W.H., G.D.L., A.J.L., Y.X.Z., B.S., J.L., C.H., Y.D., D.F.L., Y.H., S.L.H., L.Z., L.Y., X.W.J., F.F.Z., S.J.Z., F.Y., Z.M.W., Q.J.P., Z.Y.X., C.T.C. and X.J.Z. contributed to the development and maintenance of the Laser-ARTOF system and related software development. C.L.W., Y.Z., G.D.L. and J.W.H. carried out the ARPES experiment. C.L.W., Y.Z., G.D.L. and X.J.Z. analyzed the data. G.D.L., C.L.W. and X.J.Z. wrote the paper with Y.Z., L.Y., A.J.L., S.M.N. and H.M.W.. All authors participated in discussion and comment on the paper.

### **Additional information**

Supplementary information is available in the online version of the paper. Correspondence and requests for materials should be addressed to G.D.L. or X.J.Z.

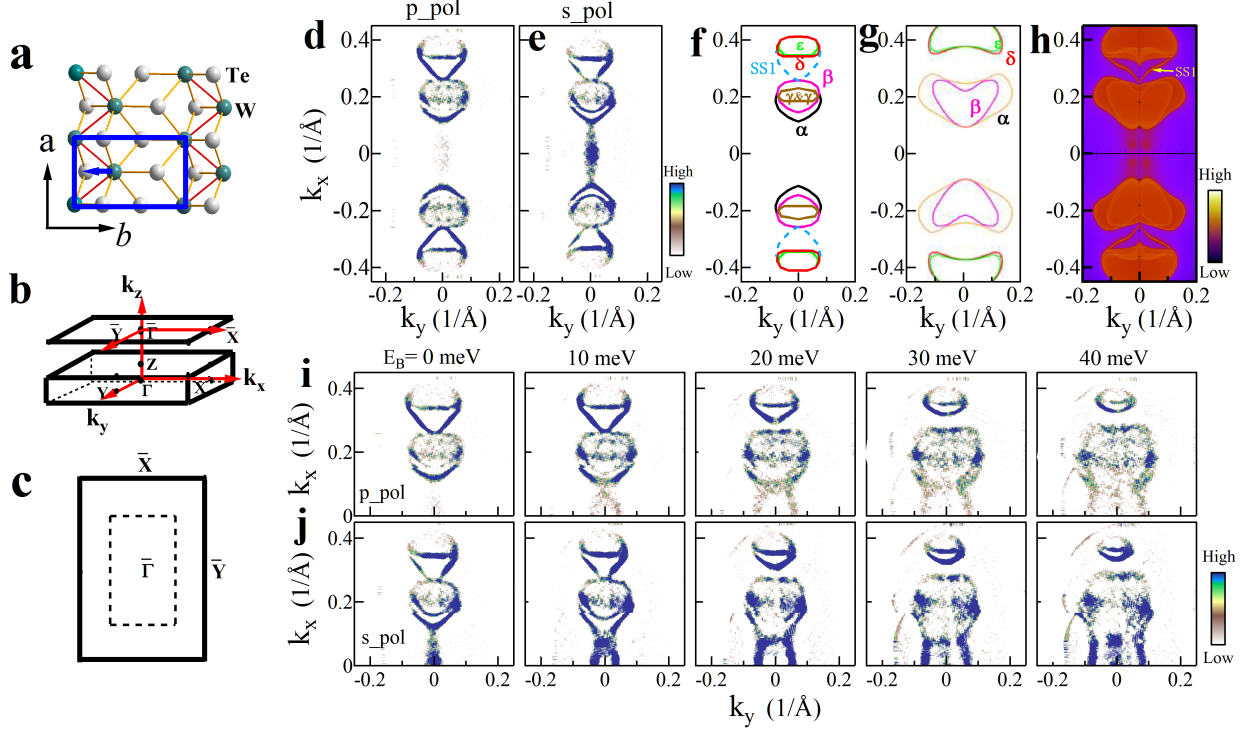


Fig. 1: **Fermi surface of  $\text{WTe}_2$  and its comparison with calculated results.** (a) Crystal structure of  $\text{WTe}_2$  in Td form with a space group  $Pmn2_1$ , viewed along the  $c$  axis (perpendicular to the stacked layers). The W-W zigzag chains are shown by the red solid line and the direction of the lattice distortion marked with the blue arrow. The unit cell is indicated by blue rectangle. (b) The bulk Brillouin zone and projected (001) surface Brillouin zone. (c) Corresponding (001) surface Brillouin zone. The dashed rectangle marks the momentum region covered in our ARPES measurements. (d) Fermi surface of  $\text{WTe}_2$  taken by ARToF-ARPES at 20 K with  $p$ -polarization geometry. The spectral weight distribution is obtained by integrating photoemission spectra at each momentum within an energy window of  $[-2.5, 2.5]$  meV with respect to the Fermi level. (e) Fermi surface of  $\text{WTe}_2$  taken by ARToF-ARPES at 20 K with  $s$ -polarization geometry. In both (d) and (e), the lower half region is obtained by symmetrizing the upper half part of the measured Fermi surface with respect to the  $\bar{\Gamma}$ - $\bar{Y}$  mirror plane. (f) Schematic of all measured Fermi surface sheets. The solid lines represent the bulk pockets, and the dashed lines represent the surface state segments. Different pockets are drawn with different colors. (g) Calculated bulk Fermi surface at  $k_z=0$ . (h) Calculated projected Fermi surface including surface states. (i) Constant energy contours of  $\text{WTe}_2$  at different binding energies measured at 20 K under  $p$ -polarization geometry. (j) Same as (i) but measured under  $s$ -polarization geometry. All the images in this figure are obtained by the second derivative of the original data with respect to energy.

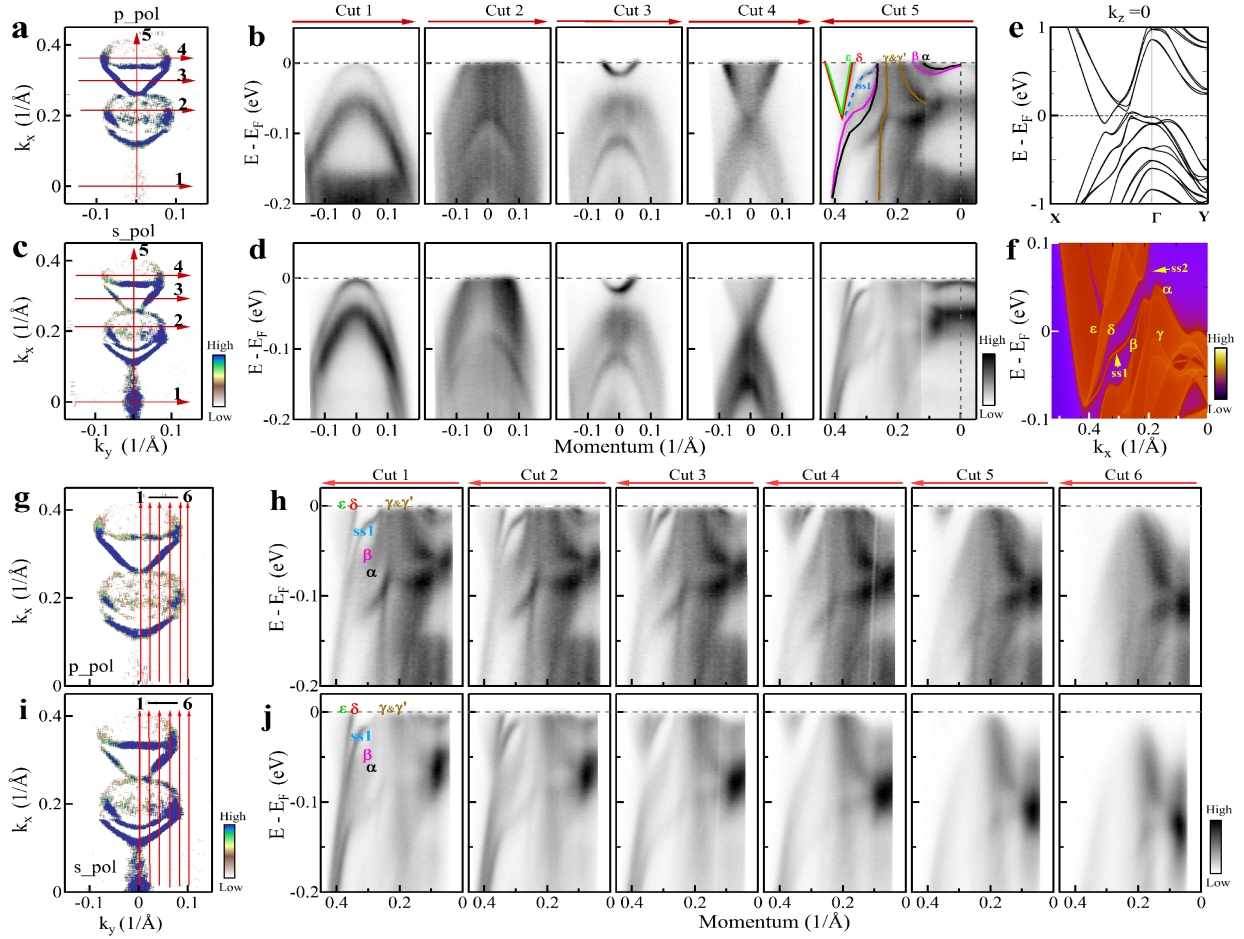


Fig. 2: **Band structures of WTe<sub>2</sub> measured along typical momentum cuts and their comparison with the band structure calculations.** (a) Fermi surface of WTe<sub>2</sub> measured at 20 K under *p*-polarization geometry. The image is obtained by the second derivative of original data with respect to energy. (b) Band structures measured along different momentum cuts 1 to 5. The location of the five momentum cuts are marked by red lines in (a). The main bands are labeled in the Cut 5 panel by lines with their colors corresponding to those of the Fermi pockets and surface state in Fig. 1f. (c) Same as (a) but measured under *s*-polarization geometry. (d) Same as (b) but measured under *s*-polarization geometry. (e) Calculated bulk band structure along X- $\Gamma$ -Y with  $k_z$  at 0. (f) Calculated band structure along  $\Gamma$ -X including surface states. (g) Fermi surface of WTe<sub>2</sub> measured at 20 K under *p*-polarization geometry. The image is obtained by the second derivative of original data with respect to energy. (h) Band structures measured along the momentum cuts marked in (g) as red lines. They show clear momentum evolution of the surface bands and the bulk bands. (i) Same as (g) but measured under *s*-polarization geometry. (j) Same as (h) but measured under *s*-polarization geometry.

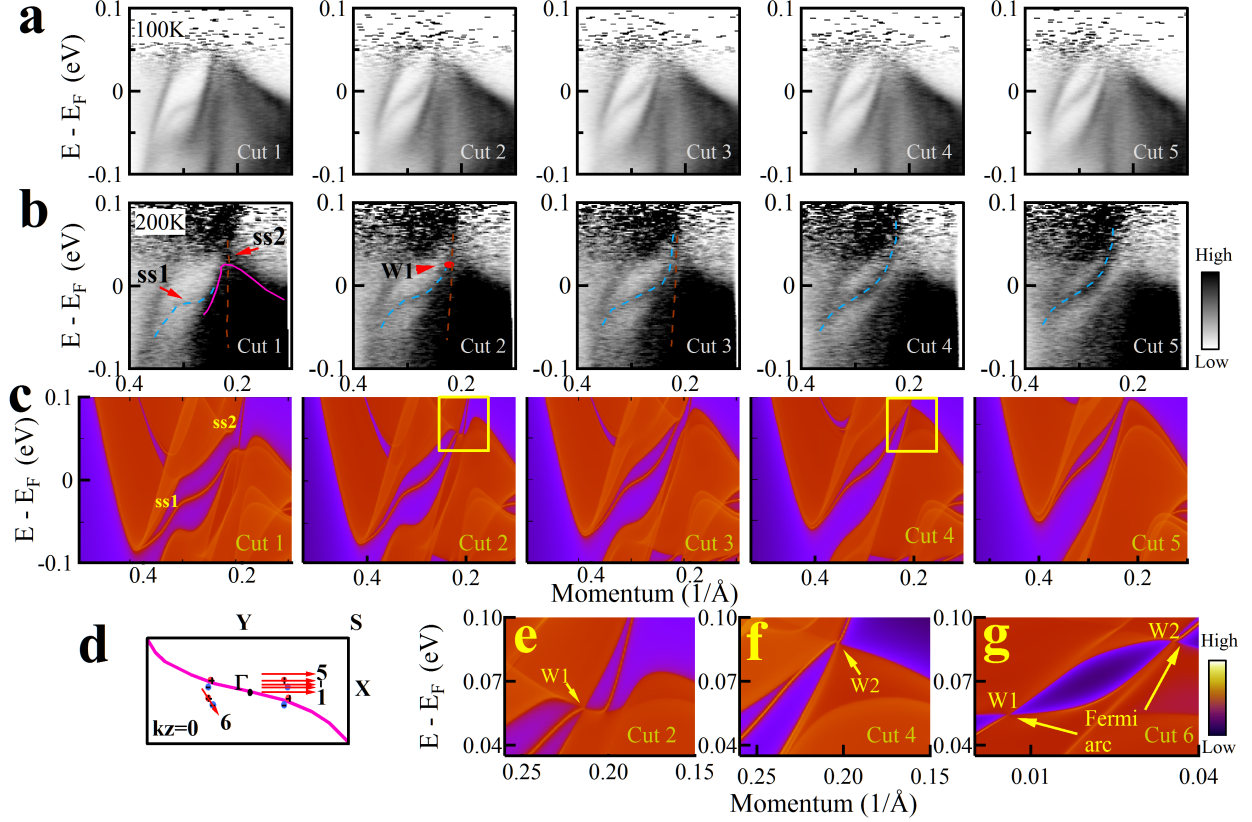


Fig. 3: **Identification of Weyl points in  $\text{WTe}_2$  through its band structure evolution.** (a and b) Band structures of  $\text{WTe}_2$  measured along different momentum cuts at 100 K and 200 K. The location of the momentum cuts 1 to 5 are marked in (d). In order to observe electronic states above the Fermi level, the images in (a) and (b) are obtained by dividing the original data with the corresponding Fermi distribution function. W1 is the momentum space position of a "candidate Weyl point". (c) The calculated band structures along the same five momentum cuts as marked in (d). (d) A schematic for the distribution of the calculated four sets of Weyl points within a bulk Brillouin zone at  $k_z=0$ : Weyl point 1 (W1) is represented by blue dots while Weyl point 2 (W2) by red dots. The chirality is marked with "+" and "-", corresponding to  $C = +1$  and  $C = -1$ . Wilson loop is shown schematically as the pink solid curve. The locations of the 5 momentum cuts are marked by red lines where Cut 2 crosses W1 Weyl point, Cut 4 crosses W2 Weyl point and Cut 6 crosses both W1 and W2 Weyl points. (e) Expanded view of the region marked by yellow rectangle in (c) for the Cut 2. Here the electron band and hole band touch at the W1 Weyl point. (f). Expanded view of the region marked by yellow rectangle in (c) for the Cut 4. Here the electron band and hole band touch at the W2 Weyl point. (g). Calculated band structure for the momentum cut 6 that crosses the two Weyl points.

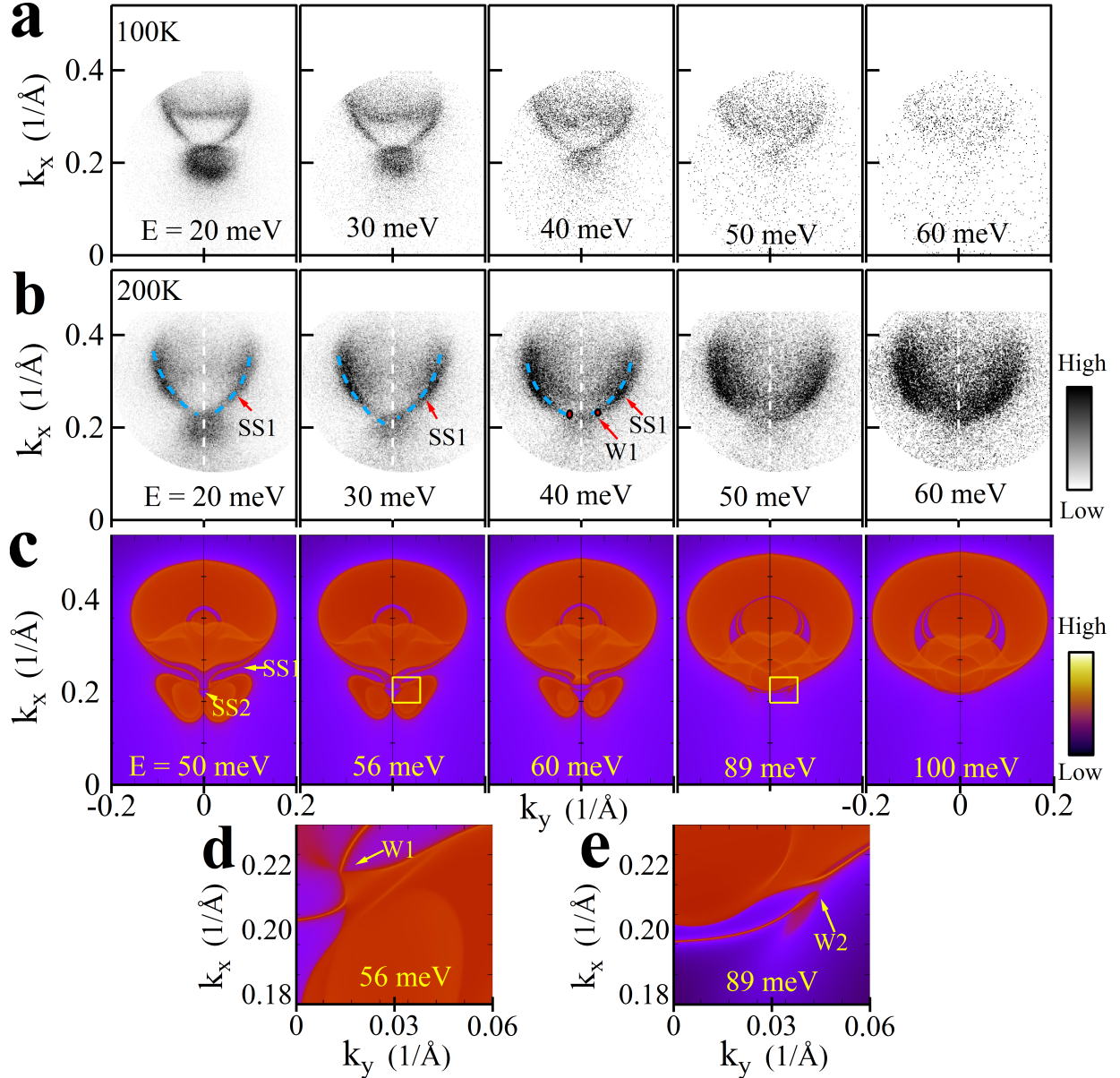


Fig. 4: **Identification of Weyl points in  $WTe_2$  through the constant energy contours.**

(a and b) Constant energy contours of  $WTe_2$  above the Fermi level measured at 100 K and 200 K. The surface state SS1 is marked as the blue dashed line. Here the 100 K data and 200 K data were taken from two separate  $WTe_2$  samples. W1 is the momentum space position of a "candidate Weyl point". (c) Calculated constant energy contours of  $WTe_2$  including the surface state above the Fermi level near the Weyl points. The surface states SS1 and SS2 are marked by the yellow arrows. (d) Expanded view of the region crossing the W1 point marked by yellow rectangle in (c) for the 56 meV energy. (e) Expanded view of the region crossing the W2 point marked by yellow rectangle in (c) for the 89 meV energy. The W1 and W2 points are marked by the yellow arrows in (d) and (e).